Symmetric-cell characterization of the redox flow battery system: Application to the detection of degradations

Mathilde Cazot, Gaël Maranzana, Jérôme Dillet, Florent Beille, Thibault Godet-Bar, Sophie Didierjean

Symmetric-cell characterization of the redox flow battery system: application to the detection of degradations

Mathilde Cazot[a,b], Gaël Maranzana[a], Jérôme Dillet[a], Florent Beille[b], Thibault Godet-Bar[b], Sophie Didierjean[a]

a. Lemta, Laboratoire d'Energétique et de Mécanique Théorique et Appliquée, UMR CNRS-Université de Lorraine n° 7563, 2 avenue de la Forêt de Haye, BP 160, F-54504 Vandœuvre-lès-Nancy, France

b. Kemiwatt, 11 allée de Beaulieu, 35708 Rennes France

ABSTRACT

A combined modelling-experiments approach is presented with the aim of determining in-situ key characteristics of a RFB. The porous electrode impedance was calculated and measured without and with a faradaic reaction, by means of a symmetric cell. The technique was applied to the specific $[Fe(CN)_6]^{3-}$ / $[Fe(CN)_6]^{4-}$ couple whose interest for RFB application is substantial. The interpretation of Electrochemical Impedance Spectroscopy (EIS) data enabled the determination of the key membrane and electrode resistances and the investigation of their evolutions during the battery operation. The effects of the cation composition in the supporting electrolyte, the carbon material and the cycling were analysed. The results gave insights on degradation mechanisms that can hinder RFB performance, and delineated the phenomena occurring during electrolyte circulation or during battery operation.

1. Introduction

Redox Flow Batteries (RFBs) are a promising solution for large-scale and low-cost energy storage necessary to foster the use of intermittent renewable sources. Unlike enclosed batteries, RFB architecture allows its energy capacity to be scaled separately from its output power. The most advanced technology is based on vanadium dissolved in acidic medium [1], but challenges with material scarcity and corrosivity motivates the investigation of other redox couples. The potential of organic or organo-metallic compounds based on plentiful metals can boost RFB to become the first energy storage reference technology. Due to its reversibility, low-cost and compatibility with an organic anolyte, the iron hexacyanide redox pair is frequently used as a catholyte option in alternatives to vanadium redox flow battery (VFB) [2]. Although this redox couple is considered as an example in terms of electrochemical properties, its use in a RFB can reshape its behavior and necessitates to review it accordingly.

To offer a competitive and reliable RFB, the evaluation of the main factors influencing its performance is requisite for targeting the full system optimization. While modelling the system is an efficient and common approach, the relevance of the results is pledged by the accuracy of input parameters that represent the intrinsic features of the system. Their determination ex-situ or in standard conditions can however lead to incorrect estimation. For instance, the charge transfer rate constant is easily measured at a plane and uniform electrode surface; nonetheless, the porous electrode structure can alter the electrochemical response of a reaction [3].

The insight of the electrode operation is particularly essential for a good understanding of the RFB system. The electrode analysis based on the model of porous electrode introduced by Newman and Tobias [4] is widely used to examine electrochemical systems [5, 6, 7, 8].

Becker et al. [9] coupled this model to the experimental EIS technique to investigate the effect of electrode material on the performance of VFB.

The physically based impedance modelling described by Zago and Casalegno [10] takes into account the different mass transfer mechanisms into the porous structure. By comparison with experimental data, their respective contribution to the total electrode resistance could be resolved.

Sun et al. [8] applied EIS to a symmetric cell equipped with a reference electrode to probe the voltage losses at the negative electrode of a VFB. Their mathematical tool considers ohmic, charge transfer and diffusion losses in the volumetric electrode. They could quantify the overvoltages resulting from each process during the electrode polarization at several operating conditions, by changing the electrolyte flow rate and electrode thickness.

Due to the complexity of the flow battery systems, simplified analytical tools are required to decouple the phenomena. Two diagnostic cell configurations exist, using only one electrolyte and inherently ruling out crossover related issues.

A single-electrolyte redox flow cell, where both electrodes are fed by a common reservoir, is a good analytical hardware to study one electrolyte in a flowing configuration at constant State Of Charge (SOC) [5, 8, 7]. Symmetric flow cells make the study more advanced: separate tanks of a same electrolyte feed the cell to allow its cycling. Several researchers have built such cells to identify the limiting electrolyte in terms of coulombic efficiency and capacity retention [11, 12], or to assess the capacity fade mechanisms of a single redox species [13, 14]. The symmetric configuration secures the electrolyte environment by removing the possibility of cross-over of the other electrolyte, and by studying the electrolyte

stability on the same porous material as in the full battery [14]. It is even possible to discriminate between the behavior of the reduced and of the oxidized forms of the electrolyte. Luo and co-workers [12] were the first to evaluate long-term cycling capability of the iron-cyanide redox pair $[Fe(CN)_6]^{3-}$ / $[Fe(CN)_6]^{4-}$ by means of a symmetric cell. They unravelled the influence of the pH on its stability. Post-analysis by Nuclear Magnetic Resonance attributed the capacity decay at high pH to a chemical degradation of the reduced form. Degradation mechanisms are difficult to identify in-situ and very few papers strive to understand them. Several papers focused on the graphite felt degradation in a VFB [15, 16, 17, 18, 19]. In all cases, cycling revealed a loss of performance partly due to electrode degradation. By post-mortem analyses such as X-ray photoelectron spectroscopy, Scanning Electron Microscopy (SEM) or electrochemical techniques, a decrease of the specific surface area along with chemical oxidation of the carbon surface and reduction of the catalytic activity of the felt could be detected.

This article relates the development of a new combined modelling-experience approach with the aim of determining in-situ key characteristics of a RFB. Based on the Newman 1-D porous electrode analysis, two versions of the impedance model are proposed, each of which describing a special configuration: when the electrode current is only capacitive or when the electrode hosts a faradaic reaction. These two conditions were reproduced experimentally by means of a symmetric cell. The models enable the interpretation of Electrochemical Impedance Spectroscopy (EIS) data to determine the key membrane and electrode resistances, and to investigate their evolutions during the battery operation. The results gave insights on degradation mechanisms that can hinder RFB performance, and delineated the phenomena occurring during electrolyte circulation or during battery operation.

The technique was applied to the specific $[Fe(CN)_6]^{3-}$ / $[Fe(CN)_6]^{4-}$ couple whose interest for RFB application is substantial. A cation-exchange membrane was used, as it prevents the crossover of the negatively charged active molecules and is very stable under alkaline conditions. The compatibility of this electrolyte on two types of porous electrodes, carbon felt or carbon paper, could be assessed. Indeed, the choice of electrode material and the related cell design is a prominent topic in RFB studies [6].

2. Impedance models of the porous electrode

In this section, the development of the electrode models from purely resistive to impedance without faradaic reaction are presented.

The modeling domain, whose schematics is given in Fig. 1, is the half-cell porous electrode located between the current collector and the membrane.

Fig. 1. Schematic of the half-cell geometry considered for modeling.

The shared assumptions of the models presented in this section are:

- The electrolyte concentration is assumed uniform inside the cell, making the problem one-dimensional in the through-plane direction along the *x*-axis.
- The half-cell is treated as isothermal.
- The electrodes material and properties are homogeneous and isotropic.
- The charges transport (electrons and ions) obeys Ohm's law. The assertion is valid when there is no concentration variation in the electrolyte solutions.

2.1. Electrode resistance

The Newman porous electrode model is a macroscopic description of the electrode relative to the properties of the liquid and solid phases constituting it. The system is considered in steady-state. The electronic current density in the solid phase j_s and the ionic current density in the solution j_e are given by:

$$j_s = -\sigma \frac{d\phi_s}{dx} \qquad (1)$$

$$j_e = -\kappa \frac{d\phi_e}{dx} \qquad (2)$$

ϕ_s and ϕ_e are the potentials of the solid and liquid phases. σ and κ are the effective conductivities of respectively the porous matrix and the electrolyte filling the pores; they take the electrode porosity and tortuosity into account.

The conservation of charge relates the electronic and ionic currents densities to the total current density I applied to the battery:

$$j_s + j_e = I \qquad (3)$$

Therefore:

$$\frac{dj_s}{dx} + \frac{dj_e}{dx} = 0 \qquad (4)$$

The faradaic reaction occurring in the pores of the electrode is located at the solution/solid interface. If averaged over a representative macroscopic volume, the divergence of the ionic current density is related to the local faradaic current density $j_F(x)$ by the specific area of the porous electrode a (expressed in m^2/m^3):

$$\frac{dj_e}{dx} = a\, j_F(x) \qquad (5)$$

According to the Butler-Volmer equation, the reaction kinetics characterized by $j_F(x)$ is exponentially dependent on the surface overpotential $\phi_s(x) - \phi_e(x)$. In the case of a porous

electrode with large specific area, the current applied only generates small local overpotentials, so that the Butler-Volmer relation can then be linearized as follows [20]:

$$j_F(x) = \frac{1}{b} j_0[\phi_s(x) - \phi_e(x)] \qquad (6)$$

With:

$$j_0 = k_0 F C_{tot} SOC^{\alpha}(1 - SOC)^{1-\alpha} \qquad (7)$$

α is the charge transfer coefficient, k_0 is the rate constant of the electrochemical reaction; $b = R\,T/n\,F$ is the Tafel slope with F Faraday's constant, T the temperature (in K), and n the number of electrons exchanged. SOC stands for the State Of Charge of the electrolyte and represented the ratio of the charged species over the total active species concentration.

At the electrode-membrane interface, the ionic current is equal to the current density I applied to the battery, whereas at the interface with the current collector the electronic current embodies the total flow of charges:

At $x = 0$, $j_e = 0$ and $j_s = I$ (8)

At $x = L$, $j_e = I$ and $j_s = 0$ (9)

The analytical resolution of this set of equations leads to the following expression of the ionic current density distribution in the electrode:

$$\frac{j_e(x)}{I} = \frac{sh(\lambda\, x/L)}{sh(\lambda)} + \frac{\kappa}{\kappa + \sigma} \frac{sh(\lambda) - sh(\lambda x/L) - sh\big(\lambda(1 - x/L)\big)}{sh(\lambda)} \qquad (10)$$

With:

$$\lambda^2 = \frac{a}{b} j_0 \left(\frac{L^2}{\kappa} + \frac{L^2}{\sigma} \right) \qquad (11)$$

The voltage drop observed between the solid phase potential at the collector and the electrolyte potential at the membrane is caused by the losses in the half-cell. The electrode resistance R_e is introduced to represent these losses inside the electrode:

$$R_e = \frac{\phi_e(x=L) - \phi_s(x=0)}{I} \qquad (12)$$

According to the solution of the model (Eq. (10)) and Eq. (1) and (2), the electrode resistance is:

$$R_e = \frac{L}{\sigma + \kappa}\left[1 + \frac{2}{\lambda\, sh(\lambda)} + \left(\frac{\sigma}{\kappa} + \frac{\kappa}{\sigma}\right)\frac{1}{\lambda\, th(\lambda)}\right] \qquad (13)$$

It can be rearranged as a function of the SOC and to introduce three new parameters:

$$\beta_1 = \sqrt{\frac{L}{\kappa}}$$
$$\beta_2 = \sqrt{\frac{L}{b} Fa\, k_0 C_{tot}} \qquad (14)$$
$$\beta_3 = \frac{\kappa}{\sigma}$$

$$R_e(SOC) = \beta_1^2 \frac{1}{1+1/\beta_3}\left[1 + \frac{2}{\lambda\, sh(\lambda)} + \left(\beta_3 + \frac{1}{\beta_3}\right)\frac{1}{\lambda\, th(\lambda)}\right] \qquad (15)$$

With:

$$\lambda^2 = \beta_1^2\, \beta_2^2\, (1+\beta_3)\, SOC^{\alpha}\, (1-SOC)^{1-\alpha} \qquad (16)$$

The electrode resistance variation with the SOC in Eq. (15), calculated with the standard parameters of Table 1, is depicted in Fig. 2A. The solid phase conductivity is either taken equal to 300 S m^{-1} (blue curve) or ideally infinite (red curve); this latter case assumes that the electrolyte conductivity is limiting compared to the solid one so that $\beta_3 \approx 0$. In this regard, R_e is simplified by:

$$R_e^{\sigma\to\infty}(SOC) = \frac{\beta_1}{\beta_2} \frac{1}{\sqrt{SOC^{\alpha}\, (1-SOC)^{1-\alpha}}\, th\left(\beta_1\, \beta_2 \sqrt{SOC^{\alpha}\, (1-SOC)^{1-\alpha}}\right)} \qquad (17)$$

Fig. 2. Electrode resistance. A) Influence of the solid phase conductivity B) Sensitivity coefficients.

Table 1. Standard effective parameters

As presented in Fig. 2A, the electrode resistance increases as the SOC varies from 50% to 100%. It would be the same between 50% and 0%. The resistance is obviously higher if the solid phase conductivity is not infinite.

The black curve in Fig. 2A depicts the difference between the resistance calculated with finite and infinite solid conductivity: it is almost constant (except at SOC close to 100%). This means that neglecting the solid phase resistance only shifts the curve downward without reshaping it.

Before using the porous electrode model for parameters determination, a preliminary sensitivity analysis must be carried out. Dimensionless sensitivity coefficients are introduced to be able to compare them:

$$S_{\beta_i} = \beta_i \frac{\partial R_e}{\partial \beta_i}\bigg|_{\beta_j} \qquad (18)$$

The sensitivity coefficients of β_1, β_2 and β_3 are presented in Fig. 2B as a function of the SOC, for the set of parameters given in Table 1 and σ =300 S m^{-1}. The graph reveals that R_e is sensitive to all parameters. However, since S_{β_1} and S_{β_2} are proportional, the two parameters cannot be deduced simultaneously from the resistance measurement. The sensitivity to β_3 is nearly constant, which confirms that the solid phase resistance can be regarded as an additional term to the electrode resistance at infinite σ. This simplification will be used in the following parts.

2.2. Electrode impedance taking into account the double layer capacitance

The dynamic perturbation of the porous electrode by EIS activates its capacitive property. In this case, the ionic current density is produced by the local faradaic current density $j_F(x)$ and by the charge / discharge of the double layer capacity:

$$\frac{\partial j_e}{\partial x} = a\, j_F(x) + C_{dl}\frac{\partial(\phi_s - \phi_e)}{\partial t} \qquad (19)$$

where C_{dl} is the electrochemical double layer capacitance of the electrode (F m^{-3}).

To interpret the EIS measurements, the electrical signals are taken as the product of two functions: one depending only of the time and the other one depending only of the space: $F(t,x) = f(x)\exp(j\omega t)$. Therefore, combined with Eq. (6), Eq. (19) becomes:

$$\frac{\partial j_e}{\partial x} = \left[a\frac{j_0}{b} + j\omega\, C_{dl}\right][\phi_s(x) - \phi_e(x)] \qquad (20)$$

The resolution is similar to the previous case. By introducing a new parameter $\beta_4 = C_{dl}L$ and considering infinite solid phase conductivity, the electrode impedance can be extended to:

$$Z_e(SOC) = \beta_1 \frac{1}{\sqrt{\beta_2^2\, SOC^{\alpha}(1-SOC)^{1-\alpha} + j\omega\,\beta_4}} \frac{1}{th\left(\beta_1\sqrt{\beta_2^2\, SOC^{\alpha}(1-SOC)^{1-\alpha} + j\omega\beta_4}\right)} \qquad (21)$$

The electrode impedance simplifies to the electrode resistance R_e at DC current, that is when $\omega \to 0$. As such, the value of R_e stands at the intercept of the x-axis in the Nyquist representation.

2.3. Electrode impedance without faradaic reaction

As it was presented by Gaumont et al. [21], the impedance model can be simplified to the specific case of $\beta_2 = 0$ when no faradaic reaction occurs in the pores; it is referred to as blocking conditions. The blocking electrode impedance, noted Z_b is only a function of the frequency:

$$Z_b = \beta_1 \frac{1}{\sqrt{j\omega\,\beta_4}} \frac{1}{th\left(\beta_1\sqrt{j\omega\beta_4}\right)} \qquad (22)$$

Z_b depends on the ionic resistance of the electrode via β_1 and on the double layer capacity in β_4. The electrode impedance tends towards 0 at very high frequency. When decreasing the frequency, the electrode impedance can be approximated by $Z_b \approx \beta_1 \frac{1}{\sqrt{j\omega\,\beta_4}}$ and the Nyquist plot features a 45° slope in the high-medium frequency region. At low frequencies, the electrode behaves like a pure capacity and appears as a vertical line in the Nyquist chart (semi-circle with infinite diameter): $Z_b^{\omega\to 0} \approx \frac{1}{j\omega\,\beta_4}$.

Fig. 3A displays the Nyquist plot of the blocking electrode impedance Z_b for the standard parameters (Table 1) giving $L/\kappa = 2\ \Omega\,\text{cm}^2$ and for $C_{dl}\,L = 6\ 10^{-4}$ F cm^{-2}. The sensitivity analysis of the impedance magnitude $|Z_b|$ depending on the frequency is shown in Fig. 3B.

The electrode impedance is sensitive to both β_1 and β_4. At low frequencies the impedance is mainly sensitive to the double layer capacity, and at medium frequency it is most sensitive to the ionic resistance. This analysis shows that the two parameters β_1 and β_4 can be deduced simultaneously from the impedance measurement providing that it is performed over a wide range of frequencies. The blocking electrode model was applied by Malifarge et al. [22] to derive electrode physical characteristics such as the pore tortuosity from the determination of the effective ionic conductivity κ in β_1. In the present study, the model was applied to a

symmetric cell filled with the supporting electrolyte to force the blocking conditions at the electrodes.

Fig 3. A) Nyquist plot of the impedance.

B) Impedance amplitude $|Z_b|$ and sensitivity coefficient to β_1 and β_4 as a function of the frequency for $L/\kappa = 2\ \Omega\ \text{cm}^2$ and $(L\ C_{dl}) = 6\ 10^{-4}\ \text{F cm}^{-2}$.

2.4. Total impedance of the symmetric cell

In this paper, the EIS data relates to the total impedance of the symmetric cell.

At high frequency, that is when the faradaic reactions are frozen out, only the first term of Eq. (13) remains in the electrode resistance. It corresponds to the resistances of the solid phase and liquid phase in parallel. With the consideration that the electronic conductivity is higher than the ionic conductivity ($\sigma >> \kappa$), the expression simplifies to the solid phase resistance $\left(R_{solid\ phase} = L/\sigma\right)$. The total impedance of the symmetric cell at high frequency comprises twice this term, added to the contact resistances $R_{contact}$ and to the membrane resistance R_m:

$$R_{HF} = 2\ R_{solid\ phase} + R_{contact} + R_m \qquad (23)$$

The sum $\left(2\ R_{solid\ phase} + R_{contact}\right)$ was experimentally assessed in a dry cell assembled without membrane and with two porous electrodes at a compression ratio of 35%. This set-up also includes a contact resistance between the felts not present in the full cell. The measurements done with one or two layers of carbon felts confirmed that it was negligible since the two materials are identical and sufficiently compressed. The value of 0.09 Ω cm² was measured with a four-probe milliohmeter. In the subsequent results, this value has been systematically subtracted from R_{HF} to isolate the membrane resistance.

The application of the aforementioned electrode models to the symmetric cell set-up induces the following assertions:

- The charge transfer coefficient α is equal to 0.5; this value is confirmed experimentally in the literature for the couple $[Fe(CN)_6]^{3-}$ / $[Fe(CN)_6]^{4-}$ [23].
- The oxidation and the reduction of the ferri/ferrocyanide species are first-order reactions and their respective kinetics follow the same electron-transfer rate k_0.

The junction potential at the electrolyte-membrane interface is neglected in this study.

Given these assumptions, the impedances of the positive and negative electrodes of the symmetric cell are the same.

Therefore, the total impedance of the cell Z_{tot} is the sum of twice the electrode impedance (Z_e or Z_b depending on the test conditions) and of R_{HF}:

$$Z_{tot} = 2\,Z_{e/b} + R_{HF} \qquad (24)$$

Z_{tot} contains several variables to determine by fitting the model to the experiments.

In the Z_e expression in Eq. (21), we chose to focus on the parameter β_2 to seek an *in-situ* estimation of $a\,k_0$, the product of the reaction rate k_0 and of the specific surface area a, which remains hard to determine [3]. β_1 being correlated to β_2, it was estimated by preliminary conductivity measurements. The sensitivity of Z_{tot} regarding R_{HF} is constant with SOC and thus uncorrelated with β_2. This made possible to estimate the membrane resistance R_m from Eq. (24). In the case of the blocking electrode conditions, the influence of the supporting electrolyte and of the electrode material on the resistances were explored through the impedance model Z_b. The parameters β_1 (related to electrolyte conductivity), β_4 (representing the double layer capacity) and R_{HF} present in the electrode impedance could be extracted concomitantly from the fitting.

In all cases, the experimental data fitting by the model was performed by a non-linear least square method implemented in Matlab with two different algorithms: trust region reflective and Levenberg-Marquardt [24].

3. Experimental

3.1. Materials and experimental setup

The electrolytes tested in the symmetric set-up were mixes of 2M NaOH and 2M KCl solutions for the blocking configuration. The active electrolyte used was composed of 0.5 M of the reduced species $K_4[Fe(CN)_6]$ dissolved in 0.2 M NaOH. The solution was half-charged in a standard flow battery to reach a SOC of 50%. The raw chemicals were all purchased from Sigma-Aldrich.

The 80 µm Aquivion ® membrane (E98-09S Solvay) was pre-treated by boiling in a solution of 1M HNO_3 at a temperature of 130°C for 2 hours, to clean the material. After cooling down, the polymer membrane was rinsed into baths of deionized water and then soaked in 1 M KOH to convert it into alkaline form.

The porous electrode either consisted of GFD 4.6 mm porous felt or one or two layers of Sigracet® GDL 38AA carbon paper, both of which provided by SGL Group. The standard thickness and porosity of the materials were respectively 4.6 mm and 94% for the felt and 0.3 mm and 82% for the carbon paper. Electrodes were used as received, but once assembled the cell was rinsed with 1M KOH before starting a new test.

The 25 cm² square cell (5x5 cm) was assembled with gilded brass plates in which 30 parallel channels (cross-section of 0.4 mm²) had been machined. The electrolytes were circulated to the cell by diaphragm pumps at a flow rate of 200 mL/min to minimize mass transport limitation.

3.2. Impedance as a function of SOC

The symmetric cell set-ups were characterized with Electrochemical Impedance Spectroscopy. In order to comply with the uniform concentration hypothesis, the spectra were performed at the open circuit voltage (OCV) over the frequency range [50 mHz ; 50 kHz] in galvanostatic mode (high-frequency limit defined from hardware constraints). The AC perturbation was set to +/- 6 mA cm^{-2}, this being a good compromise between a small value to limit concentration oscillation with faradaic processes and a value high enough to obtain a good signal to noise ratio.

When the symmetric cell contained active material, its impedance was followed according to its SOC. Starting from 50% SOC, the cell was charged sequentially at 40 mA cm^{-2} until the limit voltage of 0.9 V. Current step lengths were adapted during the charge to obtain a satisfactory resolution of the curve representing R versus the SOC. During charge, oxidation occurred at the positive half-cell, making the electrolyte charge from 50 to 100% SOC. In the same time, reduction took place at the negative electrode and the electrolyte SOC varies between 50 and 0% on this side. It was arbitrarily considered that the SOC of the symmetric cell evolved between 50 and 100% during the cycles.

A rest of 2 minutes and a GEIS measurement followed each step of charge (increasing the SOC of 5 to 10 %). Then, the cell was discharged without interruption at the same current amplitude, during a duration equal to the charge. At the end of discharge, the cell was back at its symmetric state, with both electrolytes at 50% SOC. This method of cycling based on charging and discharging the cell for an identical period of time was validated by preceding tests. They showed that with the system in use, the capacity retention was good over a few cycles. The initial SOC was then kept constant for the successive cycles at several concentrations.

A Nyquist plot of the impedance obtained for the symmetric cell at 50% SOC is presented in Fig. 4. These spectra were measured on a cell with carbon paper electrodes, with which the characteristic loops are more distinctive than with carbon felt.

Fig. 4. Complex Impedance spectrum of the symmetric cell at SOC = 50% with carbon paper electrodes for 2 flow rates. The square show the value at 100 Hz.

From the spectra, it is clear that the real component of the impedance prevails over the imaginary part. They are composed of two successive loops:

- The small arc at frequencies higher than 100 Hz (left side of the spectrum) relates to the interface where the electrochemical reaction happens; it is usually associated with an equivalent RC circuit accounting for the charge-transfer resistance and the double-layer capacity of the electrode. Even at the highest frequencies tested this loop stays open because of a low double-layer capacitance value.
- A large loop was obtained at the frequencies lower than 100 Hz (right side of the spectrum). It can be ascribed to mass transfer limitations by diffusion and convection. Spectra recorded at two electrolyte flow rates are compared in Fig. 4; the variation of the low frequency loop underpins this theory. This part of the impedance plot is not described by the electrode model developed earlier; it will not be considered in the following.

The relevant part of the spectra for this study is the mid-frequency resistance, outlined by the square in Fig. 4. According to the cell impedance given by Eq. (24), this value corresponds to the sum of the high-frequency resistance R_{HF} and of twice the electrode resistance R_e. Since the high-frequency loop remains open within the range of possible frequency scanning, R_{HF}

value is not readily available from the plot; fitting the impedance model to the R vs SOC curve paves the way for decoupling the two resistive elements R_{HF} and R_e.

The spectrum obtained with carbon paper reaches the x-axis at only one point (the square in Fig. 4) between the two loops. However, the use of carbon felt induced a level section of several points between the 2 loops. The mid-frequency resistance was thus calculated by the average of the impedance measured between 50 Hz and 200 Hz. It induced a measurement error of less than 5%. To keep the test short, the scanned frequencies were restricted to 5 medium values between 20 Hz and 1 kHz, since only this part would be needed for the model fitting.

4. Experimental results and discussion

4.1. Membrane and ionic electrode resistances

The first results scrutinize the influence of the solvent composition and of the electrode material on the cell impedance.

To that end, the symmetric cell was tested with several cationic compositions in blocking conditions, that is, without electroactive species.

A cell assembled with carbon felts was first filled with pure NaOH 2M on both sides. Controlled volumes of KCl 2M were progressively added to the solution, to make the cation ratio Na^+/K^+ vary while maintaining the total salt concentration constant to 2M. KCl salt was selected to provide the potassium cations instead of the potash KOH, because its level of purity (100%) being higher than the KOH (86.5%), any risk of membrane pollution was then excluded. At each cationic ratio, the solution was circulated during several hours with periodic EIS measurements to observe the stabilization of the spectrum, with a flow rate of 200 mL/min. The average time needed for stabilization was 4 hours. The last spectrum obtained for each electrolyte was processed for interpretation.

The Nyquist and Bode plots and the fits obtained for NaOH 2M are presented in Fig. 5. They follow the typical shape of a blocking electrode impedance. The low frequency line attributed to capacity is not completely vertical. This tilt underlines a small faradaic current created by parasitic reactions such as carbon oxidization or water reaction.

Fig. 5. Bode and Nyquist representations of the experimental EIS of a blocking symmetric cell filled with NaOH 2M (blue dots) and fitted porous electrode model (black line)

The impedance spectra obtained for all the solution compositions were fitted using Eq. (24), with the blocking electrode impedance model (Eq. 22). As mentioned before, the adjusted spectra extract the underlying values of R_m, κ and C_{dl}, each of which contained in R_{HF}, β_1 and β_4 respectively.

The double layer capacity estimated with the model is small and nearly constant over the different concentrations. All the values lie between 6 10^{-4} to 12 10^{-4} F cm^{-2}. The discrepancy originates from a non-ideal capacitive behaviour at low frequency. By relating this estimation to the electrode samples weights (measured beforehand), the average gravimetric double layer capacity value was found to be about 20 10^{-3} F g^{-1}.

Rabbow et al. [25] correlated the active surface area of a carbon felt to its total surface area and its gravimetric electrochemical double-layer capacity. They reported an electrochemical double-layer capacity of 30 10^{-3} F g^{-1} for PAN-based carbon felts with a comparable total surface area (ours is 0.4 m^2 g^{-1} according to SGL data). The value reported by Rabbow et al. is consistent with our estimate.

For the blocking electrode, R_{HF} is obtained at the spectrum intercept (or extrapolated intercept) with the real axis in the Nyquist chart. It is therefore possible to monitor this

resistance variation with the Na^+/K^+ ratio of the solution. The results are outlined in Fig. 6A. As the solid phase resistance is not affected by the nature of the electrolyte, its value (0.09 Ω cm²) was subtracted from the total measurement. Fig. 6A. evidences the membrane resistance dependency on the cationic charge carriers: R_m increases with the addition of K^+ in the solvent (from left to right on the diagram). This reveals that the K^+ ions are less mobile in the membrane than the Na^+, and from the Na^+-form to the K^+-form, R_m increased by at least 30%.

These findings show a good agreement with the results presented by Shi et al. [26] and by Kusoglu et al. [27]. These authors reported that the ionic conductivity of Nafion® membrane in K^+ form is lower than in Na^+ form. They also reported the very complex effects on the membrane behaviour in high concentrated electrolyte solutions containing multiple cations and anions.

Fig. 6. A) Membrane resistance: variation with NaOH / KCl concentration. B) Effective ionic conductivity of the electrolyte: variation with NaOH / KCl concentration.

After the cell impedance stabilized with the KCl 2M salt, the membrane was replaced by another pre-treated sample; the data relative to this sample appear in blue in Fig. 6A. The new membrane showed a higher resistance of 1.88 Ω cm². When the solution is changed back to pure NaOH (from right to left on the chart), the detected R_m follows a decrease similar to with the previous membrane, but cannot reach a value as low as before, even after several hours of circulation. The hysteresis response alludes to an “historical effect” of the membrane

exposure to mobile cations. If first soaked in a solvent containing sodium ions, the membrane will keep a low resistance even when the surrounding is later replaced by K^+ ions. On the other hand, a membrane directly exposed to K^+ displays a higher resistance even with the presence of sodium charge carriers thereafter. The resistance discrepancy between the two samples is more acute in KCl 2M than in NaOH 2M. This suggests that the membrane cannot be fully converted to another cationic form by the sole driving force of diffusion at room temperature.

The results draw the conclusion that not only the choice of the material for the separator is critical, since one ionomer can display enhanced performances with a specific cationic charge carrier. The supporting electrolyte must be composed in regard to the active material but also the nature of the membrane. Nevertheless, the experiment did not exactly mimic the real battery configuration since no current was drawn from the cell and conclusions need to be moderated with respect to this. Indeed, the migration mechanisms induced by a potential gradient could reshape the membrane behavior.

The bulk ionic conductivities of NaOH 2M and KCl 2M measured at 25°C are respectively 26.5 S m^{-1} and 18.7 S m^{-1}. The effective ionic conductivities extracted from the impedance fits are presented in Fig. 6B. These effective estimates actually enclose the disturbance generated by the porous geometry of the electrode. Their divergence from the bulk conductivity corresponds to the correction factor describing the porous structure and equals 0.8-0.85. By using the classic Bruggeman correction factor $\varepsilon^{1.5}$, the porosity of the felt compressed at 35% was estimated to ε =90%. The value is coherent with the material open porosity of 94% (SGL data).

Fig. 6B highlights a progressive increase of the effective ionic conductivity with the Na^+ / K^+ ratio incrementation. The variation is still distorted from a straight line since the dilute

solution theory cannot be strictly applied to these highly-concentrated solutions. The blue bars correspond to the second membrane experiment; as expected, the fitted ionic conductivity values are reproducible thus confirming the accuracy of the method.

Several electrode materials were surveyed with the present method in order to verify the coherence of the determined parameters and to foresee the effect of the electrode type on the cell performance. Hereafter, each electrode of the symmetric cell was either composed of one carbon felt or one or two layers of carbon paper. The solvent used was NaOH 2M.

All the assemblies were compressed with the same ratio of 33%. The open porosity of the carbon paper given by the manufacturer is 82%. By solid volume conservation, the porosity of the compressed paper is 73%.

Fig. 7 compares the EIS spectra of the 3 cell configurations. The 45° high-frequency slope is distorted when using the carbon paper, which reduce the fitting quality. The spectra display a similar membrane resistance for any electrode nature. The estimated electrode resistance and the corresponding effective ionic conductivity are gathered in the Table 2 below along with the electrode thickness.

Fig. 7. EIS of a symmetric cell made of felt or diffusion layers. Left: measurement and best fit (black curves). Right: zoom at high frequency.

Table 2. Electrode resistance and effective ionic conductivity from blocking electrode results

The electrode resistance unsurprisingly varies according to the electrode material mostly because of its thickness. Since it is almost doubled when measured for one or two layers of

carbon paper, the resulting ionic conductivity is independent of the number of carbon layers. Nevertheless, the obtained value of 5 $S.m^{-1}$ constitutes only 20% of the real solution conductivity, whereas the fraction should obey $\varepsilon^{1.5}$ (62% for the carbon paper) as it was the case with the felt electrode.

This irregularity could be ascribed to the effect of the flow field machined in the end plate. The parallel channels would behave as an electrode of thickness equal to the channel depth (0.4 mm), and thus alter the electrode resistance detected. Indeed, considering the total thickness of carbon paper and channel results in an effective conductivity close to the predicted value. On the other hand, the channel influence was not detected for the carbon felt. The felt being a soft material, it can partially fill the void spaces of the channels once compressed. It is also thicker and more porous than the carbon paper: the bypass flow in the channels is insignificant thanks to a low pressure drop through the electrode [6].

In summary, the flow field + carbon paper configuration gives higher ionic electrode resistance (comparatively to its thickness) than the carbon felt. As for its suitability for hosting a redox reaction, it is determined in the following sections.

4.2. From purely capacitive to faradaic behaviour and interaction with the active material

The transition from a blocking electrode to an active electrode hosting electrochemical reactions was observed by the gradual addition of reactive species. The experience was performed in a symmetric cell with a flow rate of 200 mL/min. At each step, EIS measurements were repeated over a few hours to verify if the system was at equilibrium. The Nyquist plots evolution with the cationic composition is given in Fig. 8 for carbon felt (A) and carbon paper (B).

The cell was first filled with the solvent NaOH 2M; $[Fe(CN)_6]^{4-}$ powder was then added on one side of the cell to obtain a concentration of 0.5M of ferrocyanide. This step is denoted by

"ferro" in the legend. One, and then both sides of the cell were replaced with a solution composed in equal proportion of the ferri/ferrocyanide species corresponding to a 50% SOC (0.25M of each form); these steps are mentioned as "ferri/ferro". This protocol was applied to a cell assembled with carbon felts. The first and last solution configurations were also tested on a cell assembled with one layer of carbon paper at each electrode.

In Fig. 8, the mention of "d+1" indicates the spectra obtained after 1 day of circulation. The squared data point out the impedance at 100 Hz.

Fig. 8. Impedance spectra evolution with addition of active species. A) Carbon felt B) Carbon paper.

Generally, the addition of the active species tends to increase the cell resistance. Indeed, the counter-ion of ferrocyanide is K^+, so that this increase relates to the aforementioned influence of the cation on R_m. The left graph highlights that the 45° slope remains even with the presence of ferrocyanide on one side but fades away when this side was filled with a mixture of ferri/ferrocyanide. It gives way to a circular shape that still terminates vertically. It is only when both sides of the cell were supplied with a redox couple that the full semi-circle replaces the blocking electrode line at decreasing frequency. The diagram on the right gives evidence that a similar evolution is observed with carbon paper. Nevertheless, the final complex impedance plot obtained for the two electrode materials is different.

As mentioned previously, the ohmic cell resistance resolved at the high-frequency intercept is lower with the thinner carbon paper. The EIS shape at high frequency also exhibits a facilitated charge transfer at the carbon paper. This matches the suggestion of Pezeshki et al. [6] that the activity of the graphitized paper is greater than the carbon felt in VFB. By

comparison of the exchange current density which contains the specific surface area, the electrode thickness and the rate constant, the difference between the two materials is actually not that obvious in the work of Becker et al. [9].

At low frequency, the response of the two types of electrode is also contrasting. With carbon felt, the shape of a tiny loop can barely be noticed while with the carbon paper configuration, the low frequency loop dominates the spectrum.

This second semicircle is often put down to critical mass transport limitation that is mitigated by increased electrolyte velocity within the pores. This can be achieved by changing the flow rate as already highlighted in Fig. 4 but is also a consequence of the porous structure. The carbon paper features concurrently a reduced thickness and porosity compared to the felt. As asserted by pressure drop measurements in [6], this hinders the portion of the solution flowing through the electrode. The electrolyte instead bypasses the porous material via the channels. On the contrary, the structure of the carbon felt facilitates the electrolyte penetration into the pores, reduces the bypass flow in the channels and promotes a uniform electrolyte distribution.

The difference between carbon felt and carbon paper were less critical in the study presented by Darling and Perry [5]. Aside from the porous structure itself, several external factors can account for the discrepancy of the two electrodes responses. The critical diffusion loss observed with the carbon paper could also be amplified by the flow field geometry employed in our study; the parallel channels have already proved to be inefficient compared to other designs such as serpentine, because of lack of forced convection within the electrode [5].

Furthermore, Maranzana et al. [28] evidenced that concentration oscillation could also create parasitic effects in the low frequency semicircle and lead to an overestimation of the mass transport losses. This oscillation may spread along the parallel channels from the inlet to the

outlet, and thus be exacerbated with the carbon paper layout. Finally, the diaphragm pumps used for the study could also interfere with the signals at low frequency.

The complex impedance spectrum was recorded again after one day of circulation in the two cell configurations. The plot is significantly shifted on the x-axis towards increased resistances in the case of the carbon felt, while it is completely unchanged with the carbon paper. The charge-transfer loop expanded in the case of the felt electrode: it entails a significant increase of the charge transfer loss, whereas R_{HF} did not increase as critically. Complementary tests not presented here confirmed a systematic increase of the cell resistance of about 10% during the first day of circulation with carbon felt after what it stabilized, while it remained nearly constant when the cell was composed of carbon paper. Deeper analyses are required to elucidate this phenomenon, even though several hypotheses can already be put forth: a contaminant could be released from the felt and block some of the membrane ionic sites, or the electrolyte interaction with the felt could impede the electrode activity.

4.3. Electrode resistance variation with SOC

With the purpose of unravelling the resistance increase observed with carbon felts after a day of circulation, the cell impedance spectra was followed relative to the SOC of the ferri/ferrocyanide electrolyte, by applying sequential charges to the symmetric cell. Fig. 9 shows its mid-frequency resistance as a function of the SOC at several days of circulation.

The curves were recorded at several experimental times (number of days specified in the legend). The electrolyte was circulated continuously in the cell for 3 days. Test 1 reports the response of the freshly assembled cell. After Test 3, 100 charge / discharge cycles were performed; Test 4 depicts the curve evolution after these 5 days of cycling.

All the curves show the same characteristic shape as the theory presented in Fig. 2A, with a curvature appearing at high SOC. The curves were assumed to take a symmetrical shape if extended towards 0% SOC.

Fig. 9. Electrode resistance as a function of the SOC and best fit (black curves)

Table 3. Evolution with time of R_m and $a\ k_0$ from curve fitting of Fig. 9.

As unveiled in the previous section, the cell resistance sharply increased by 10% after a few hours of flowing (between Test 1 and Test 2). The 3 days of circulation slightly reshaped the curve (Test 3) with no further resistance increase. The curves were fitted to Eq. (17) and (24) to derive the variables R_m and $a\ k_0$ by the least squares method. Their estimates are presented in Table 3. They reveal that the detected resistance increase was actually not caused by the performance degradation of the membrane, but the major contribution lies in the diminution of $a\ k_0$. The justification of the performance degradation can be refined: the electrolyte circulation impairs either or both of the total active surface area and the reaction rate constant, at the electrode level. Surface functional sites can be blocked or even degraded by a mechanism specific to this catholyte/electrode material coupling.

As Tests 1 to 3 suggest, this interaction seems to be triggered by the sole circulation of the solution.

To our knowledge, no published paper reports a compatibility issue between the iron-cyanide pair and a carbon felt that would happen even without current drawn from the system.

Possibly correlated explanations found in the literature relate to electrochemical reaction or battery cycling. Concerning the electrode itself, Derr et al. [29] observed with a VFB an early

degradation during the first 20 cycles that they partly attributed to the electrochemical degradation of the carbon felt. Cycling gives rise to corrugated surface accompanied by a loss of fibre surface area. In their study, the loss of active surface was not reversible.

The $[Fe(CN)_6]^{3-}$ /$[Fe(CN)_6]^{4-}$ couple also presents a complex reaction process that involves adsorption phenomena on the electrochemical surface, as reported with a gold [30] or a platinum electrode [31].

After the 100 charges/discharges cycles (Test 4), the characterization curve shifted downwards and its shape evolved slightly. The model fitting points out that the kinetic product $a\,k_0$ recovered its initial value, and in the meantime, the membrane resistance increased of about 9%: the cycling, unlike the circulation of electrolytes, increases the membrane resistance. It also suggests that kinetics diminution observed during circulation is reversible: flowing current through the cell could unlock the functional groups of the electrode or wipe away the active material that had been adsorbed. These are only suggestions and would require further analysis such as ex-situ characterization to be confirmed.

It is worth mentioning that the information on capacity retention is still missing in Fig. 8. The cycling could partially modify the SOC of the two electrolytes. A small capacity fade was observed during 100 cycles, being however less than the rate of 0.2% per cycle announced by Luo et al. [12]. They concluded about the instability of the ferricyanide/ferrocyanide redox couple in alkaline conditions. They used a similar set-up, with the only difference being their solutions initially at SOC 100 and 0, so that they cycled them through the entire capacity of each tank. The divergence of the results found herein with the work of Luo et al. is the resistance evolution during cycling; while they displayed increased ohmic losses with time, results of Test 4 in Fig. 9 demonstrates no cell-level degradation after 100 cycles. Luo et al. [12] proposed a mechanism of hydrolysis that could account for the capacity decay, yet did not correlate it with the resistance increase observed in their voltage curves. Furthermore, they

did not mention any precaution against light exposure, while the degradation of potassium ferrocyanide by light has long been known. Reinhard et al. [32] detailed this photooxidation process. In the present work, the electrolyte was protected from light exposure throughout the study, to prevent any UV-triggered deterioration. The cell resistance remaining low after the cycles negates any possible pollution in the cell (except the one attributed to the membrane), nor a species precipitation that would decrease ionic conductivity.

The exact explanation of apparent capacity fade must be addressed with complementary study. A likely hypothesis is the effect of active species crossover through the membrane, since at the charged state of the symmetric cell, the concentration gradient of ferrous and ferric forms is highest. Preliminary tests diagnosed a critical membrane permeability for the less negatively charged ferricyanide form, as mentioned in [33].

Influence of the electrolyte concentration

Subsequent to Test 4, the reservoirs were diluted two times with NaOH 2M, to reach lower active species concentrations. This experiment is referred to as "aged set-up", since it is performed on the symmetric cell after cycling. After each dilution, the characterization curve was plotted. Fig. 10 overlays the data for the three concentrations: $C_1 = 0.5$ M, $C_2 = 2/3\ C_1$ and $C_3 = 1/3\ C_1$. Table 4 presents the corresponding fitted parameters obtained with the model (black-line plots in Fig. 10).

Fig. 10. Electrode resistance as a function of the SOC and fitted model (black curves). Influence of the active species concentration on an aged set-up.

Table 4. Evolution with time of R_m and $(a\ k_0)$ from curve fitting of Fig. 10

For this aged set-up, the model fit to the experimental data attributes no change to R_m nor to $a\,k_0$ after dilution. The gradual resistance increase observed in Fig. 10 for the lower concentrations only stems from a lower conductivity, whose measured value was input to the model.

The dilution experiment was replicated with a new symmetric cell and freshly prepared electrolyte. The parameters determined for this experiment correspond to the rows "new set-up" of Table 4. The membrane resistance for C_1 is very reproducible with Test 1 (Table 3), while $a\,k_0$ have the same order of magnitude than for the previous test. The small discrepancy is attributed to the specific surface area a that could vary between two samples of electrode.

The fitting with the new cell underlines an evolution of both R_m and $a\,k_0$ with the 3 concentrations tested (from the highest C_1 to C_3). R_m decreases when diluting the active material with a solution of NaOH. The potassium being the counter-ion of the iron-cyanide, the dilution implies an increase of the Na^+/K^+ ions ratio. As demonstrated earlier, this can account for an enhanced membrane conductivity. This effect was not observed with the membrane after cycling; R_m had already stabilized at a higher value and could not recover an enhanced performance by changing its ionic form.

Regarding the kinetics product, its variation in the case of the new set-up would draw the misleading conclusion of a linear dependency with the catholyte concentration. This is instead a time-dependent effect, pertaining again to the 10% resistance increase observed after a few hours of circulation, since the experiment of dilutions has a run time of several hours.

5. Conclusion

The present study successfully implements a method coupling a porous electrode model to specific experimental configurations to unravel the causes of performance degradation in RFB. The method dealt with the ohmic and charge-transfer resistance contributions of a symmetric cell containing the $[Fe(CN)_6]^{3-}$ /$[Fe(CN)_6]^{4-}$ pair. We developed a pure capacitive electrode impedance model in order to quantify electrode physical properties and evaluate the ionic membrane affinity. The membrane conductivity was enhanced by 30% by using sodium rather than potassium ions. The electrode impedance description was then extended to faradaic behavior by adding the iron-cyanide redox couple to the symmetric set-up. The cell resistance was monitored over time either during circulation of the electrolyte or during cycling.

A performance degradation corresponding to a 10% electrode resistance increase was observed on a carbon felt. According to the fitting results, this was linked to a diminution of the product $a\,k_0$ during the first day of circulation, after which it stabilized. It underlines a process degrading the active surface area or hampering the electron-exchange kinetics. This phenomenon is specific to the interaction electrolyte/porous electrode, since it was not detected when changing the electrode material to carbon paper.

On the other hand, cycling the cell broke in the membrane, whose resistance increased by 9% in 100 cycles. This modification appears to be permanent. In contrast, the kinetics factor $a\,k_0$ recovered its initial value after cycling, suggesting a reversible pollution. Finally, a small capacity decay was observed with the catholyte, however not correlated to material degradation at first glance. It was speculated to be a crossover issue.

Acknowledgements

The authors want to acknowledge the French company Kemiwatt for the close collaboration on this topic, and the French ANRT for financial support.

References

[1] A. Parasuraman, T. M. Lim, C. Menictas and M. Skyllas-Kazacos, "Review of material research and development for vanadium redox flow battery applications," *Electrochimica Acta,* vol. 101, pp. 27-40, 2013.

[2] P. Leung, A. A. Shah, L. Sanz, C. Flox, J. R. Morante, Q. Xu, M. R. Mohamed, C. Ponce de León and F. C. Walsh, "Recent developments in organic redox flow batteries: A critical review," *Journal of Power Sources,* vol. 360, pp. 243-283, 2017.

[3] J. Friedl and U. Stimming, "Determining Electron Transfer Kinetics at Porous Electrodes," *Electrochimica Acta,* vol. 227, pp. 235-245, 2017.

[4] J. Newman and C. Tobias, "Theoretical Analysis of current distribution in porous electrodes," *Journal of the electrochemical society,* vol. 109, pp. 1183-1191, 1962.

[5] R. M. Darling and M. L. Perry, "The influence of electrode and channel configurations on flow battery performance," *Journal of the Electrochemical Society,* vol. 161, pp. A1381-A1387, 2014.

[6] A. M. Pezeshki, R. L. Sacci, F. M. Delnick, D. S. Aaron and M. M. Mench, "Elucidating

effects of cell architecture, electrode matarial, and solution composition on overpotentials in redox flow batteries," *Electrochimica Acta,* vol. 229, pp. 261-270, 2017.

[7] J. D. Milshtein, K. M. Tenny, J. L. Barton, J. Drake, R. M. Darling and F. R. Brushett, "Quantifying Mass Transfer Rates in Redox Flow Batteries," *Journal of The Electrochemical Society,* vol. 164, pp. E3265-E3275, 2017.

[8] C. Sun, F. M. Delnick, D. S. Aaron, A. B. Papandrew, M. M. Mench and T. A. Zawodzinski, "Resolving Losses at the Negative Electrode in All-Vanadium Redox Flow Batteries Using Electrochemical Impedance Spectroscopy," *Journal of the Electrochemical Society,* vol. 161, pp. A981-A988, 2014.

[9] M. Becker, N. Bredemeyer, N. Tenhumberg and T. Turek, "Kinetic studies at carbon felt electrodes for vanadium redox-flow batteries under controlled current density conditions," *Electrocimica Acta,* pp. 12-24, 2017.

[10] M. Zago and A. Casalegno, "Physically-based impedance modeling of the negative electrode in All-Vanadium Redox Flow Batteries: insight into mass transport issues," *Electrochimica Acta,* vol. 248, pp. 505-517, 2017.

[11] K. Gong, F. Xu, J. B. Grunewald, X. Ma, Y. Zhao, S. Gu and Y. Yan, "All-Soluble All-Iron Aqueous Redox-Flow Battery," *ACS Energy Letters,* vol. 1, pp. 89-93, 2016.

[12] J. Luo, A. Sam, B. Hu, C. DeBruler, X. Wei, W. Wang and T. L. Liu, "Unraveling pH dependent cycling stability of ferricyanide/ferrocyanide in redox flow batteries," *Nano Energy,* vol. 42, pp. 215-221, 2017.

[13] M.-a. Goulet and M. J. Aziz, "Flow Battery Molecular Reactant Stability Determined by Symmetric Cell Cycling Methods," *J. Electrochem. Soc.,* 2018.

[14] J. Milshtein, J. L. Barton, R. Darling and F. Brushett, "4-acetamido-2,2,6,6-

tetramethylpiperidine-1-oxyl as a model organic active compound for nonaqueous flow batteries," *Journal of Power Sources,* vol. 327, pp. 151-159, 2016.

[15] P. Mazur, J. Mrlik, J. Pocedic, J. Vrana, J. Dundalek, J. Kosek and T. Bystron, "Effect of graphite felt properties on the long-term durability of negative electrode in vanadium redox flow battery.," *Journal of Power Sources,* vol. 414, pp. 354-365, 2019.

[16] I. Derr, A. Fetyan, K. Schtjajew and C. Roth, "Electrochemical analysis of the performance loss in all vanadium redox flow batteries using different cut-off volatges.," *Electrochimica Acta,* vol. 224, pp. 9-16, 2017.

[17] O. Nibel, S. Taylor, A. Patru, E. Fabbri, L. Gubler and T. Schmidt, "Performance of Different Carbon Electrode Materials: Insights into stability and Degradation under Real Vanadium redox Flow Battery Operation Conditions.," *Journal of the Electrochemical Society,* vol. 164, pp. A1608-A1615, 2017.

[18] I. Derr, D. Przyrembel, J. Schweer, A. Feytan, J. Langner, J. Melke, M. Weinelt and C. Roth, "Electroless chemical aging of carbon felt electrodes for all-vanadium redox flow battery (VFB) investigated by electrochemical impedance and X-ray photoelectron spectroscopy," *Electrochimica Acta,* vol. 246, pp. 783-793, 2017.

[19] A. Pezeshki, R. Sacci, G. Veith, T. Zawodzinski and M. Mench, "The Cell-in-series method: A technique for Accelerated Electrode Degradation in Redox Flow Batteries.," *Journal of the Electrochemical Society,* vol. 163, pp. A5202-A5210, 2016.

[20] Q. Chen, M. R. Gerhardt and M. J. Aziz, "Dissection of the Voltage Losses of an Acidic Quinone redox Flow Battery," *Journal of the Electrochemical Society,* vol. 164, pp. A1126-A1132, 2017.

[21] T. Gaumont, G. Maranzana, O. Lottin, J. Dillet, S. Didieerjean, J. Pauchet and L. Guétaz,

"Measurement of protonic resistance of catalyst layers as a tool for degradation monitoring," *International Journal of Hydrogen Energy,* vol. 42, pp. 1800-1812, 2017.

[22] S. Malifrage, B. Delobel and C. Delacourt, "Determination of Tortuosity Using Impedance Spectra Analysis of Symmetric Cell," *Journal of the Electrochemical Society,* vol. 164, pp. E3329-E3334, 2017.

[23] X. Zhang, J. Leddy and A. Bard, "Dependence of rate constant of heterogeneous electron transfer reactions on viscosity," *J. Am. Chem. Soc. Gas Phase Ion Chem.,* vol. 107, pp. 3719-3721, 1985.

[24] D. W. Marquardt, "An algorithm for least-squares estimation of nonlinear parameters," *J. Soc. Ind. Appl. Math.,* vol. 11, p. 431, 1963.

[25] T. J. Rabbow and A. H. Whitehead, "Deconvolution of electrochemical double layer capacitance between fractions of active and total surface area of graphite felts.," *Carbon N. Y.,* vol. 111, pp. 782-788, 2017.

[26] S. Shi, A. Z. Weber and A. Kusoglu, "Structure-transport relationship of perfluorosulfonic-acid membranes in different cationic forms," *Electrochimica Acta,* vol. 220, pp. 517-528, 2016.

[27] A. Kusoglu and A. Z. Weber, "New Insights into Perfluorinated Sulfonic-Acid Ionomers," *Chemical Reviews,* vol. 117, pp. 987-1104, 2017.

[28] G. Maranzana, J. Mainka, O. Lottin, J. Dillet, A. Lamibrac, A. Thomas and S. Didierjean, "A proton exchange membrane fuel cell impedance model taking into account convection along the air channel: on the bias between frequency limit of the impedance and the slope of the polarization curve," *Electrochimica acta,* vol. 83, pp. 13-27, 2012.

[29] I. Derr, M. Bruns, J. Langner, A. Fetyan and J. Melke, "Degradation of all-vanadium redox flow batteries (VFB) investigated by electrochemical impedance and X-ray photoelectron spectroscopy : Part 2. electrochemical degradation," *Journal of Power Sources,* vol. 325, pp. 351-359, 2016.

[30] L. F. Macia, M. Petrova and A. Hubin, "ORP-EIS to study the time evolution of the [Fe(CN)6]3- /[Fe(CN)6]4- reaction due to adsorption at the electrochemical interface," *Journal of Electroanalytical Chemistry,* vol. 737, pp. 46-53, 2015.

[31] M. Stieble and K. Juettner, "Surface blocking in the redox system Pt / [Fe(CN)6]3-, [Fe(CN)6]4-.," *Journal of Electroanalytical Chemistry and Interfacial Electrochemistry,* vol. 290, pp. 163-180, 1990.

[32] M. Reinhard, T. J. Penfold, F. A. Lima, J. Rittmann, M. H. Rittmann-Franck, R. Abela, I. Tavernelli, U. Rothlisberger, C. J. Milne and M. Chergui, "Photooxidation and photoaquation of iron hexacyanide in aqueous solution: a picosecond X-ray absorption study.," *Structural Dynamics,* vol. 1, 2014.

[33] D. G. Kwabi, K. Lin, Y. Ji, E. F. Kerr, M.-A. Goulet, D. D. Porcellinis, D. P. Tabor, D. A. Pollack, A. Aspuru-Guzik, R. G. Gordon and M. J. Aziz, "Alkaline Quinone Flow Battery with Long Lifetime at pH 12," *Joule,* vol. 2, pp. 1894-1906, 2018.

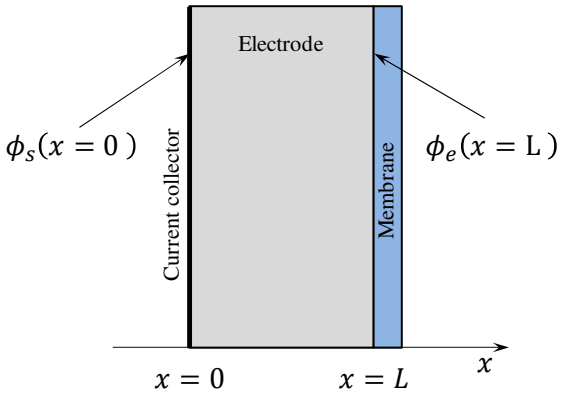

Fig. 1. Schematic of the half-cell geometry considered for modeling.

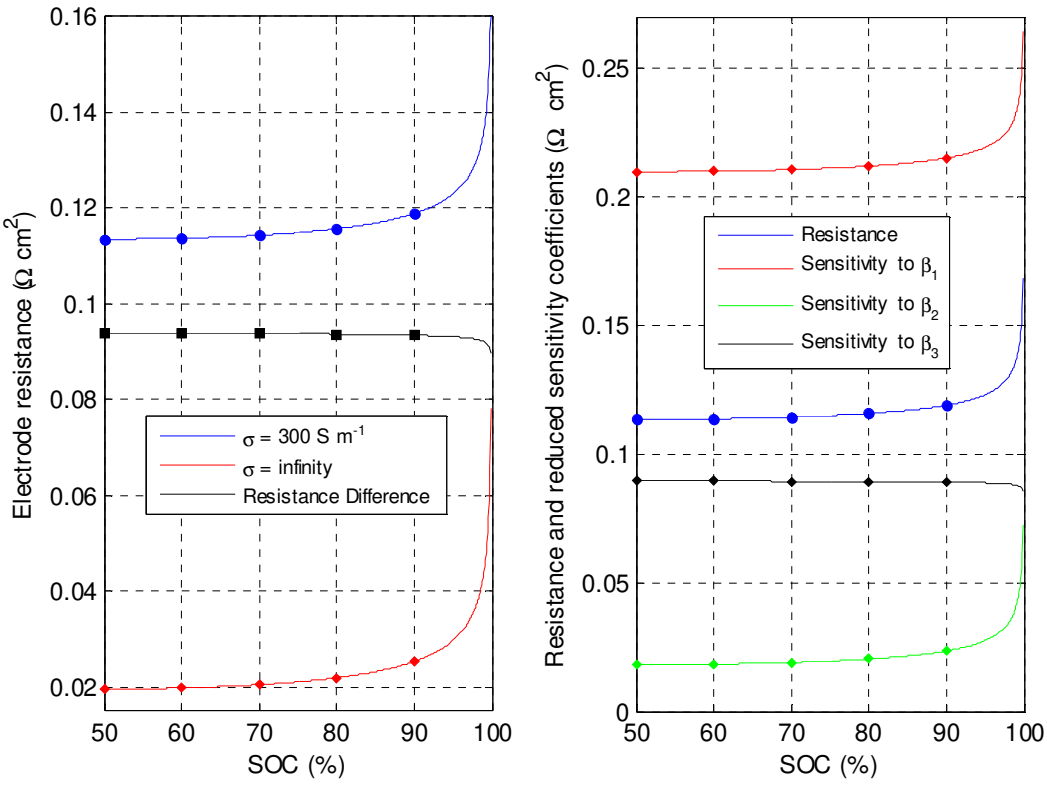

Fig. 2. Electrode resistance. A) Influence of the solid phase conductivity B) Sensitivity coefficients.

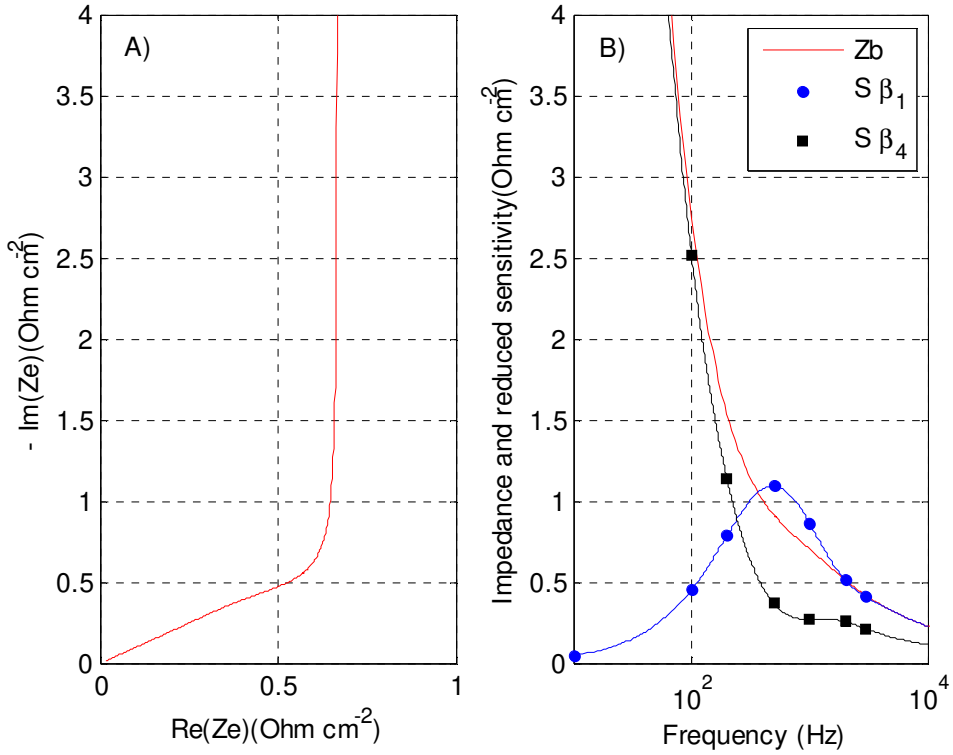

Fig 3. A) Nyquist plot of the impedance.

B) Impedance amplitude $|Z_b|$ and sensitivity coefficient to β_1 and β_4 as a function of the frequency for $L/\kappa = 2\ \Omega\ \text{cm}^2$ and $(L\ C_{dl}) = 6\ 10^{-4}\ \text{F cm}^{-2}$.

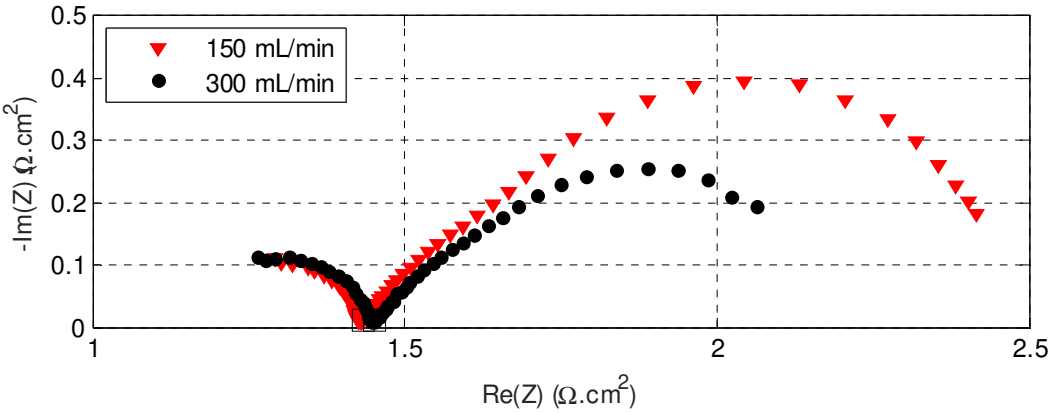

Fig. 4. Complex Impedance spectrum of the symmetric cell at SOC = 50% with carbon paper electrodes for 2 flow rates. The square show the value at 100 Hz.

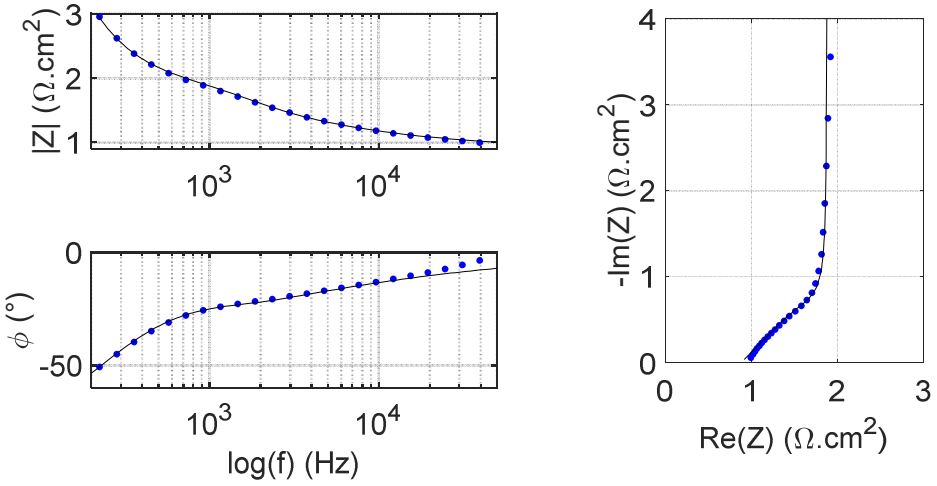

Fig. 5. Bode and Nyquist representations of the experimental EIS of a blocking symmetric cell filled with NaOH 2M (blue dots) and fitted porous electrode model (black line)

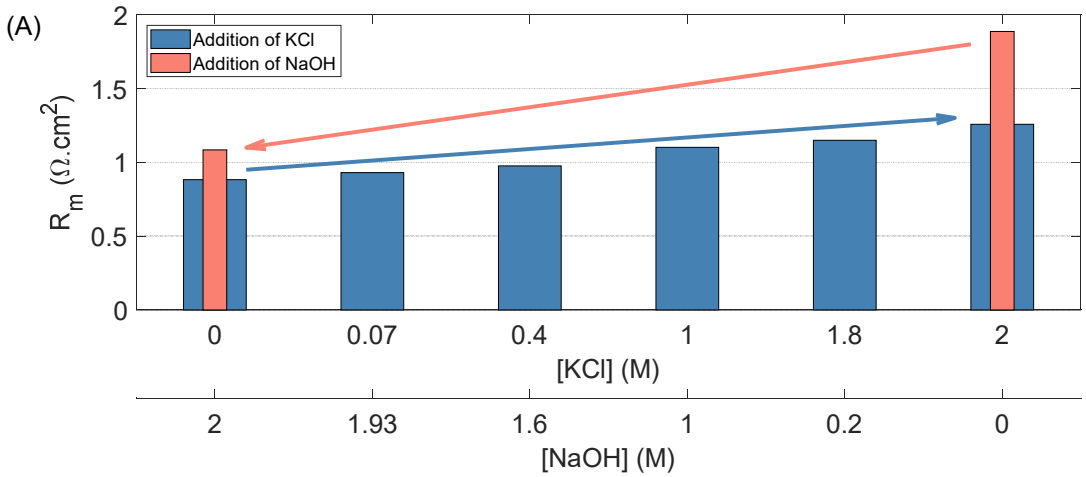
(A)
Addition of KCl
Addition of NaOH
R_m (Ω.cm^2)
2
1.5
1
0.5
0
0
0.07
0.4
1
1.8
2
[KCl] (M)
2
1.93
1.6
1
0.2
0
[NaOH] (M)

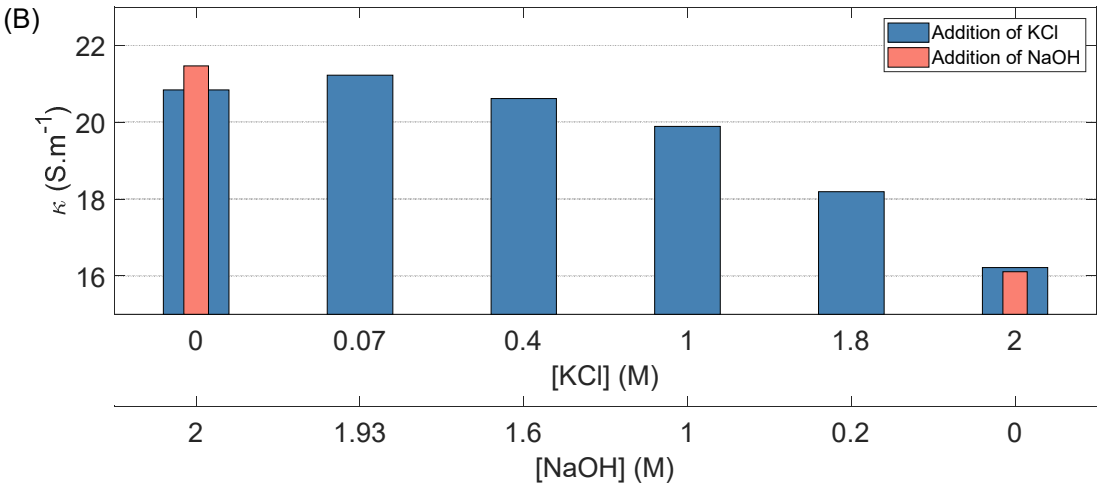
(B)
Addition of KCl
Addition of NaOH
κ (S.m^{-1})
22
20
18
16
0
0.07
0.4
1
1.8
2
[KCl] (M)
2
1.93
1.6
1
0.2
0
[NaOH] (M)

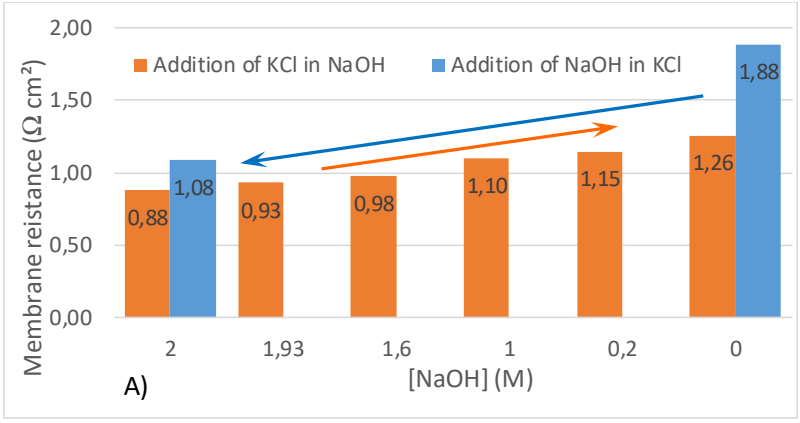
Addition of KCl in NaOH
Addition of NaOH in KCl
Membrane reistance (Ω cm^2)
2,00
1,50
1,00
0,50
0,00
0,88
1,08
0,93
0,98
1,10
1,15
1,26
1,88
2
1,93
1,6
1
0,2
0
[NaOH] (M)
A)

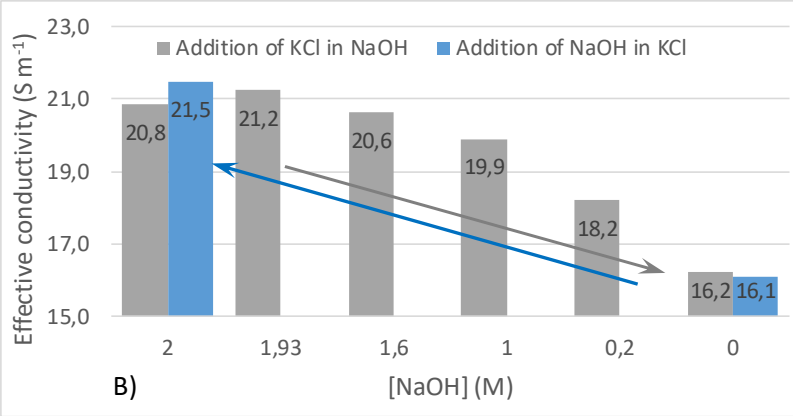

Fig. 6. A) Membrane resistance: variation with NaOH / KCl concentration. B) Effective ionic conductivity of the electrolyte: variation with NaOH / KCl concentration.

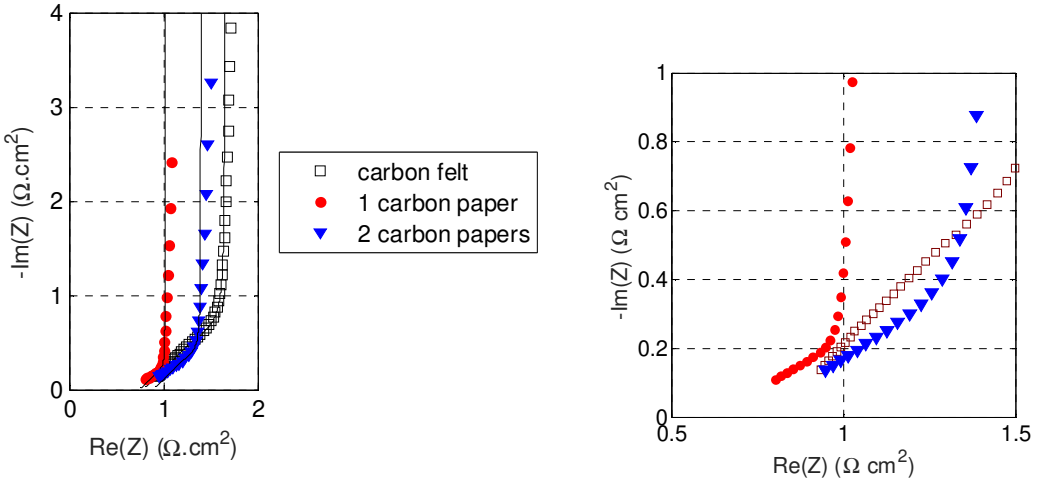

Fig. 7. EIS of a symmetric cell made of felt or diffusion layers. Left: measurement and best fit (black curves). Right: zoom at high frequency.

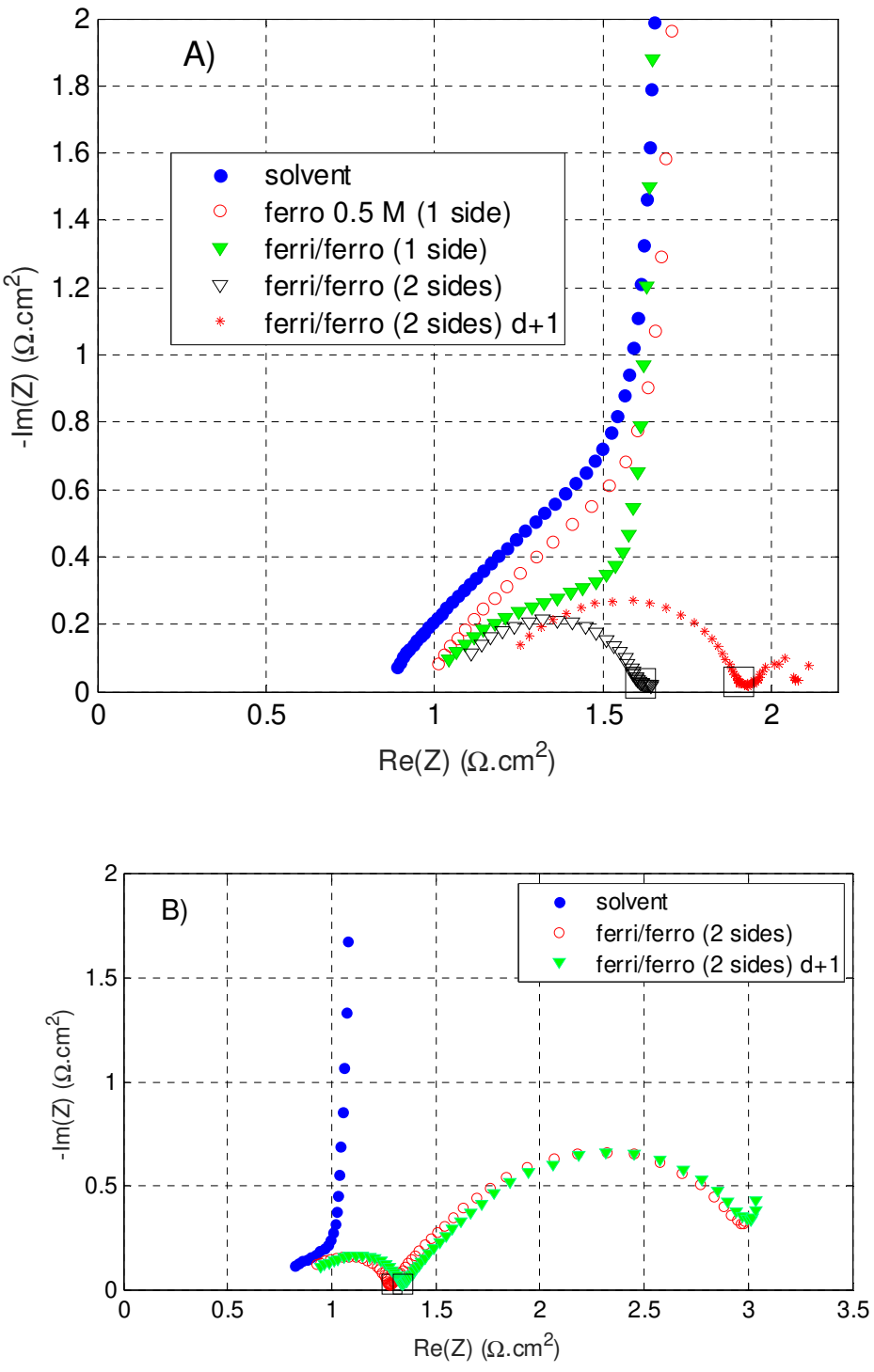

Fig. 8. Impedance spectra evolution with addition of active species. A) Carbon felt B) Carbon paper.

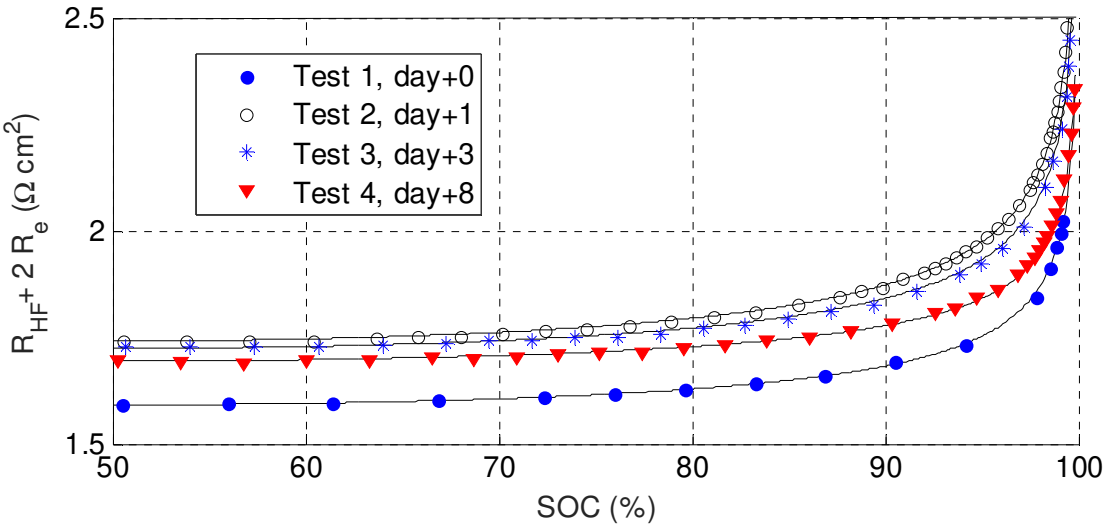

Fig. 9. Electrode resistance as a function of the SOC and best fit (black curves)

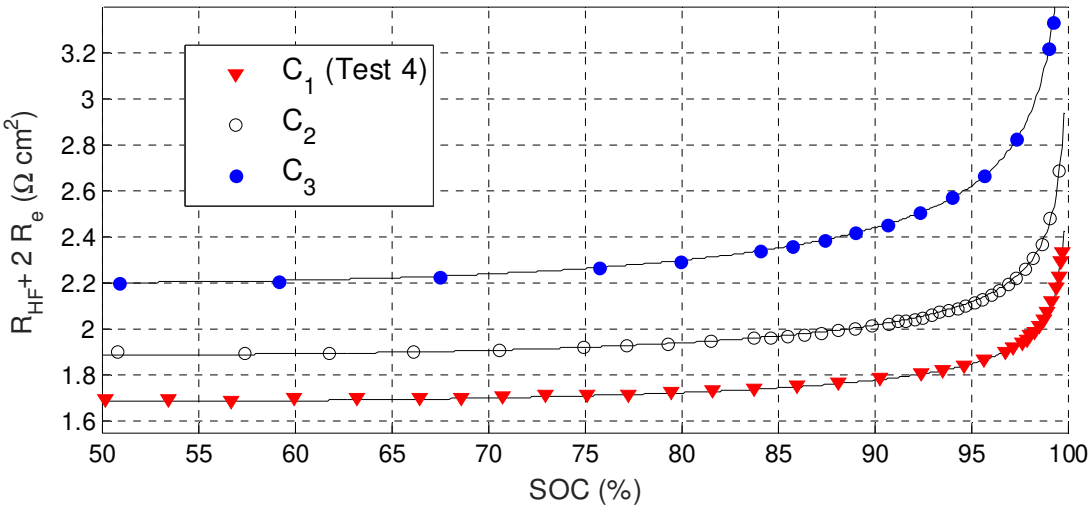

Fig. 10. Electrode resistance as a function of the SOC and fitted model (black curves). Influence of the active species concentration on an aged set-up.

Table 1. Standard effective parameters

L m	C_{tot} mole m^{-3}	κ S m^{-1}	T K	a m^2 m^{-3}	k_0 m s^{-1}	α
3 10^{-3}	0.5 10^3	15	300	100 10^3	15 10^{-5}	0.5

Table 2. Electrode resistance and effective ionic conductivity from blocking electrode results

	Carbon felt	1 layer of carbon paper	2 layers of carbon paper
Compressed Electrode thickness (m)	3 10^{-3}	0.2 10^{-3}	0.4 10^{-3}
Electrode resistance (Ω cm²)	1.44	0.42	0.77
Effective ionic conductivity (S m^{-1})	21	5	5

Table 3. Evolution with time of R_m and $a\ k_0$ from curve fitting of Fig. 9.

	R_m (Ω cm²)	$a\ k_0$ (s^{-1})
Test 1	1.18	0.33
Test 2 (1 day)	1.19	0.16
Test 3 (3 days)	1.22	0.2
Test 4 (3 days + 100 cycles)	1.28	0.33

Table 4. Evolution with time of R_m and $(a\ k_0)$ from curve fitting of Fig. 10

	Parameters	C_1 =0.5 M	C_2 =0.33 M	C_3 =0.17 M
Aged set-up	R_m (Ω cm²)	1.28	1.34	1.29
	$a\ k_0$ (s^{-1})	0.327	0.306	0.271
New set-up	R_m (Ω cm²)	1.20	1.16	1.08
	$a\ k_0$ (s^{-1})	1.42	0.70	0.33